Natural Image Statistics for Mouse Vision

² Authors: Luca Abballe¹ and Hiroki Asari^{2*}

3 Affiliations:

1

1. Department of Biomedical Engineering, Sapienza University of Rome, Rome RM,

5 00185, Italy

- ⁶ 2. Epigenetics and Neurobiology Unit, EMBL Rome, European Molecular Biology
- ⁷ Laboratory, Monterotondo RM, 00015, Italy

* **Corresponding author:** Hiroki Asari, E-mail: asari@embl.it

⁹ Acknowledgments: This work was supported by the European Molecular Biology Laboratory

¹⁰ (H.A.). EMBL IT Support is acknowledged for provision of computer and data storage servers.

¹¹ We thank all the members of the Asari lab at EMBL Rome for many useful discussions.

Author contributions: L.A. collected and processed the image data sets. H.A. designed the
 study, analyzed the results, and wrote the manuscript.

¹⁴ **Competing interests:** The authors declare no competing financial interests.

Abballe and Asari

1

15 Abstract

The mouse has dichromatic color vision based on two different types of opsins: short (S)- and 16 middle (M)-wavelength-sensitive opsins with peak sensitivity to ultraviolet (UV; 360 nm) and 17 green light (508 nm), respectively. In the mouse retina, cone photoreceptors that predominantly 18 express the S-opsin are more sensitive to contrasts and denser towards the ventral retina, 19 preferentially sampling the upper part of the visual field. In contrast, the expression of the 20 M-opsin gradually increases towards the dorsal retina that encodes the lower visual field. Such 21 a distinctive retinal organization is assumed to arise from a selective pressure in evolution to 22 efficiently encode the natural scenes. However, natural image statistics of UV light remain 23 largely unexplored. Here we developed a multi-spectral camera to acquire high-quality UV 24 and green images of the same natural scenes, and examined the optimality of the mouse retina 25 to the image statistics. We found that the local contrast and the spatial correlation were both 26 higher in UV than in green for images above the horizon, but lower in UV than in green for 27 those below the horizon. This suggests that the dorsoventral functional division of the mouse 28 retina is not optimal for maximizing the bandwidth of information transmission. Factors besides 29 the coding efficiency, such as visual behavioral requirements, will thus need to be considered to 30 fully explain the characteristic organization of the mouse retina. 31

Abballe and Asari

32 Introduction

Sensory systems have been considered to be adapted to the statistical properties of the 33 environment through evolution [1]. Animals encounter different types of sensory signals 34 depending on their natural habitats and lifestyles, and this can serve as an evolutionary driving 35 force for each species to optimize its sensory systems for processing those signals that appear 36 more frequently and are relevant for survival [2]. The optimality of the sensory processing has 37 been broadly supported from an information theoretic viewpoint of coding efficiency [3, 4]. In 38 particular, various physiological properties of sensory neurons can be successfully derived from 39 learning efficient codes of natural images or natural sounds, such as separation of retinal outputs 40 into ON and OFF channels [5], Gabor-like receptive fields of visual cortical neurons [6], and 41 cochlear filter banks [7]. Such computational theories and statistical models are, however, often 42 limited to generic features of the sensory processing, and fail to account for species-specific fine 43 details partly due to a lack of proper data sets of natural sensory signals. 44

In the past decade, the mouse has become a dominant model for studying the visual 45 system mainly because of the wide availability of experimental tools [8]. Compared to other 46 mammalian model animals such as cats and primates, however, the mouse vision has certain 47 distinctive properties. For example, mice are dichromats as many other mammals are, but 48 their retina expresses ultraviolet (UV)-sensitive short (S)-wavelength sensitive opsins and 49 green-sensitive middle (M)-wavelength sensitive opsins [9–11]. While UV vision is common 50 in amphibians, birds and insects, it has not been identified in mammals except for a few 51 species including rodents [12–14]. Moreover, the mouse retina has no fovea but a prominent 52 dorsoventral gradient in the expression pattern of the two opsins [10, 15–17]. A vast majority 53 of the mouse cone photoreceptors (\sim 95%) co-express the two opsins but with a dominant 54 expression of S- and M-opsins in the ventral and dorsal parts of the retina, respectively 55 [9, 10, 18, 19]. This makes the upper visual field more sensitive to UV than green, and vice 56 versa for the lower visual field [20]. It is natural to assume that this functional segregation of 57 the mouse vision has evolved due to an adaptation to the natural light distribution as the sunlight 58 is the major source of UV radiation. It remains unclear, though, how optimal the mouse visual 59 system is to natural scene statistics per se. 60

Abballe and Asari

While natural image statistics have been extensively studied thus far [1, 21], those outside 61 the spectral domain of human vision remain to be fully explored [2, 18, 22–24]. Here we thus 62 developed a multi-spectral camera system to sample high-quality images that spectrally match 63 the mouse photopic vision, and analyzed the statistics of the UV and green image data sets to 64 test the optimality of the sampling bias in the mouse retina along the dorsoventral axis [9, 10, 18, 65 19]. We identified distinct statistical properties in the UV and green channels between the upper 66 and lower visual field images; however, these image statistics were not necessarily consistent 67 with what the efficient coding hypothesis would predict from the functional organization of the 68 mouse retina. 69

70 Materials and Methods

71 All data and codes are available upon request.

72 Multi-spectral camera

73 Design

We built a multi-spectral camera system based on a beam-splitting strategy [25, 26] to acquire 74 images of the same scenes with ultraviolet (UV)- and green-transmitting channels that match 75 the spectral sensitivity of the mouse photopic vision (Fig 1A) [9–11]. The light coming from 76 a commercial camera lens (Nikon, AF Nikkor 50 mm f/1.8D) was collimated with a near-77 UV achromatic lens (effective focal length, 50 mm; Edmund Optics, 65-976) and split with 78 a dichroic filter (409 nm; Edmund Optics, 34-725). The reflected light, on the one hand, passed 79 through a UV-selective filter set (HOYA U-340 and short-pass filter at 550 nm; Edmund Optics, 80 84-708) and formed the UV images focused on the first global-shutter camera (Imaging Source, 81 DMK23UX174) with a near-UV achromatic lens (effective focal length, 50 mm; Edmund 82 Optics, 65-976). The transmitted light, on the other hand, passed through a band-pass filter 83 (500±40 nm; Edmund Optics, 65-743) and a lens (Edmund Optics, 65-976), and formed the 84 green images sampled by the second camera (Imaging Source, DMK23UX174). To maximize 85

Abballe and Asari

4

the dynamic range of the two camera sensors (used with the same settings), we attenuated the light intensity of the green channel using an absorptive neutral density (ND) filter (optical density: 1.0, 1.3, 1.5, 1.8, or 2.0) on a filter wheel (Thorlabs, LTFW6) because the sunlight has much higher power in green than in UV (Fig 1B). The optical components are all mounted with standard light-tight optomechanical components (Thorlabs, 1-inch diameter lens tubes).

A recent study employed a similar design but with a fisheye lens to study the "mouse-view" 91 images [22]. Our design has the following advantages over a panoramic camera design [22–24] 92 to sample high-quality image patches suitable for image statistics analysis. First, we chose a 93 small field of view (11.3 degrees horizontally and 7.3 degrees vertically; 0.006 degrees/pixel) 94 to minimize image distortion, and a large field of depth (the smallest aperture size on the 95 Nikon lens, f/22) to maximize areas in focus. This also allowed us to adjust camera settings 96 (exposure length) to fully capture the dynamic range of individual scenes. Second, we chose a 97 high-performance camera sensor (Sony, IMX174 complementary metal-oxide-semiconductor; 98 CMOS) that has high quantum efficiency ($\sim 30\%$ at 365 nm; $\sim 75\%$ at 510 nm), high dynamic 99 range (73 dB; 12 bit depth), high pixel resolution (1920-by-1200 pixels), and linear response 100 dynamics (Fig 1A, inset) [27-29]. 101

102 Spectral analysis

The spectral sensitivity of the multi-spectral camera system (Fig 1B) was calculated by convolving the relative transmission spectra of the optics for each channel with the spectral sensitivity of the camera sensor (Sony, IMX174 CMOS) [29]. The relative transmission spectra were measured with a spectrometer (Thorlabs, CCS200/M; 200–1000 nm range) by taking the ratio of the spectra of a clear sunny sky (indirect sunlight) with and without passing through the camera optics.

For a comparison, we modelled the spectral sensitivity of the mouse visual system by convolving the transmission spectra of the mouse eye [30] with the absorption spectra of the mouse cone photoreceptors (Fig 1B). We used a visual pigment template [31] with the center frequency at 360 nm and 508 nm to simulate the short (S)- and middle (M)-wavelength-sensitive opsins in the mouse retina, respectively [9–11].

Abballe and Asari

Image acquisition

In total, we collected 232 images of natural scenes without any artificial object in the suburbs 115 of Lazio/Abruzzo regions in Italy from July 2020 to May 2021. All the images were acquired 116 using a custom-code in Matlab (Image Acquisition Toolbox) without any image correction, such 117 as gain, contrast, or gamma adjustment. The two cameras were set with the same parameter 118 values adjusted to each scene, such as the exposure length, and a proper ND filter was chosen 119 for the green channel so that virtually all the pixels were within the dynamic range of the 120 camera sensors (see examples in S2 Fig). Thus, our image data sets have no underexposed 121 pixels and only a negligible number of overexposed pixels (0.0011% of pixels in 2 UV images 122 and 0.0007% of pixels in 6 Green images). This is critical because the presence of under- or 123 over-exposed pixels will skew the image statistics. 124

¹²⁵ When acquiring images, the camera system was placed on the ground to follow the ¹²⁶ viewpoint of mice. The following meta-data were also recorded upon image acquisition: date, ¹²⁷ time, optical density of ND filter in the green channel, weather condition (sunny; cloudy), ¹²⁸ distance to target object (short, within a few meters; medium, within tens of meters; or ¹²⁹ long), presence/absence of specific objects (animals; plants; water), and camera elevation angle ¹³⁰ (looking up; horizontal; looking down). We also took a uniform image of a clear sunny sky ¹³¹ (indirect sunlight) as a reference image for vignetting correction (see below Eq.(1)).

All the images were taken under ample natural light during the day. Although we did not 132 measure the exact illuminance Φ of the environment, we expect that the lighting condition was 133 on the order of 10^3 – 10^5 lux (i.e., $\Phi = 10^7$ – 10^9 photons/ μ m²/s). Assuming the mouse pupil 134 diameter $d_{pupil} = 0.5$ mm, the eye diameter $d_{eye} = 4$ mm, the transmittance of the eye optics 135 T = 0.5, and the light collection area of a photoreceptor $A_{\text{photoreceptor}} = 0.5 \ \mu\text{m}^2$, the photon 136 flux on individual photoreceptors can then be estimated as $\Phi \cdot A_{\text{pupil}} / A_{\text{retina}} \cdot T \cdot A_{\text{photoreceptor}} = 10^4 - 10^4$ 137 10^6 photons/photoreceptor/s, where $A_{\text{pupil}} = \pi \left(d_{\text{pupil}}/2 \right)^2$ is the pupil area and $A_{\text{retina}} =$ 138 $4\pi \left(d_{\text{eve}}/2 \right)^2/2$ is the total area of the retina internally covering a half of the eye. Here we 139 cannot then exclude a possible activation of rods in the mouse retina because they have similar 140 absorption spectra to the M-opsin expressing cones (peak sensitivity at 498 and 508 nm, 141 respectively) [9, 32] and may escape from saturation even at $10^7 \text{ R}^*/\text{rod/s}$ [33]. However, the rod 142

Abballe and Asari

6

system is likely optimized to work in the scotopic condition, and thus less affected by the natural
image statistics in the photopic condition. In the mouse retina, rods are indeed distributed more
densely (~97% of all photoreceptors) and rather uniformly [34].

Given the average cone density $\rho_{cone} = 12,400 \text{ cells/mm}^2$ [34], the sampling resolution (or the "pixel size") of the mouse visual system is on the order of 0.25 degrees $(= 180/(\sqrt{\rho_{cone}} \cdot \pi d_{eye}/2))$ for photopic vision), and can go as high as 0.05 degrees if rod photoreceptors are also involved (average density, 437,000 cells/mm² [34]; or average diameter of 1.4 μ m [35]). The spatial resolution of the acquired images (0.006 degrees/pixel) is thus good enough to cover the pixel size of the mouse vision.

152 Image registration

The raw images from the two cameras (12 bit depth saved in the 16 bit grayscale Portable Network Graphic format, 1920-by-1200 pixels each) were pre-processed to form a registered image in Matlab (Image Processing Toolbox). First, we corrected the optical vignetting by normalizing the pixel intensity of the raw image $I_{raw}(x, y)$ for each channel by the ratio of the pixel and the maximum intensities of the reference image $I_{ref}(x, y)$:

$$I_{\text{corrected}}(x,y) = I_{\text{raw}}(x,y) \cdot \frac{\max\left[I_{\text{ref}}(x,y)\right]}{I_{\text{ref}}(x,y)}.$$
(1)

We next applied a two-dimensional median filter (3-by-3 pixel size) to remove salt-and-pepper noise from the corrected images for each channel. Then we applied a projective transformation based on manually selected control points to register the UV image to the green image. Finally, we manually cropped the two images to select only those areas in focus. The cropped images resulted in the pixel size ranging from 341 to 1766 pixels (2.0–10.6 degrees) in the horizontal axis and from 341 to 1120 pixels (2.0–6.7 degrees) in the vertical axes (see examples in Fig 2). We never changed the image resolution.

Abballe and Asari

165 Image analysis

We analyzed the first- and second-order image statistics of the obtained natural scenes in 166 UV and green channels because the retina is not sensitive to higher-order statistics [36, 37] 167 (but see S4 Fig for higher-order statistics). Here we excluded a small set of the horizontal 168 images (N = 15) from the analysis, and focused on the following two major image groups: 169 1) looking-up images taken with a positive camera elevation angle (N = 100), presumably 170 falling in the ventral retina and thus perceived in the upper part of an animal's visual field; 171 and 2) looking-down images with a negative camera elevation angle (N = 117) perceived 172 in the lower visual field (i.e., the dorsal retina). To ensure the separation between the image 173 categories, we calculated the relative light intensity along the horizontal and vertical axes of 174 each image category (S1 Fig). Specifically, we first corrected the pixel values of each image 175 with the exposure length and the ND filter attenuation, and then normalized them by the mean 176 pixel intensity value of all images. For the population analysis, the images were then aligned 177 to the center in horizontal axes for all images, while to the top edge, center, or bottom edge in 178 vertical axes for the lower, horizontal, upper visual field image categories, respectively. For each 179 image data set, we used a sign-test to compare the image statistics parameter values between 180 the UV and green channels (Figs 3-6; significance level, 0.05). All image analysis was done in 181 Matlab (Mathworks). 182

183 Light intensity normalization

The visual system adapts its sensitivity to the range of light intensities in each environment [38, 39]. We thus first normalized the pixel intensity of each UV and green image to have the intensity value ranging from zero to one (by subtracting the minimum value of the image, followed by the division by the maximum value), and then calculated the histogram (bin size, 0.01) to compare the normalized intensity distributions of the UV and green images for the upper and lower visual fields (Fig 3A,B).

Abballe and Asari

190 Local contrast

¹⁹¹ To calculate the local statistical structure of the normalized intensity images (Fig 3C,D and ¹⁹² S3 Fig), we used the second-derivative (Laplacian) of a two-dimensional Gaussian filter:

$$LoG(x,y) = \frac{1}{\pi\sigma^4} \left(1 - \frac{x^2 + y^2}{2\sigma^2} \right) \exp\left[-\frac{x^2 + y^2}{2\sigma^2} \right],$$
 (2)

8

with the standard deviation $\sigma = 5, 10, 20, 40$ pixels for the spatial range $x, y \in [-3\sigma, 3\sigma]$. Here we chose a rather arbitrary size of the filter width (0.18--1.44 degrees) because natural image statistics are scale invariant (S3 Fig) [1, 21]. The local contrast distribution was then fitted to the two-parameter Weibull distribution:

$$w(x) = \beta \gamma |x|^{\gamma - 1} \exp\left[-\beta |x|^{\gamma}\right],\tag{3}$$

where x is the local contrast value, $\beta > 0$ is the scale parameter (width) of the distribution, and $\gamma > 0$ is the shape parameter (peakedness). In particular, larger β and smaller γ values indicate wider and more heavy-tailed distributions, respectively, hence higher contrast in the images. Sign-tests were used to compare these parameter values between UV and green images (Fig 3E–H).

202 Achromatic and chromatic contrast

To analyze the achromatic contrast of our image data sets (Fig 4), we calculated the root mean square (RMS) contrast $C^*_{RMS}(x, y)$ for each channel of normalized intensity images [22]:

$$\mathbf{C}^*_{\mathrm{RMS}}(x,y) = \frac{\sigma^*(x,y)}{\mu^*(x,y)},\tag{4}$$

where $\mu^*(x, y)$ and $\sigma^*(x, y)$ are the mean and standard deviation of a circular image patch (radius, 30 pixels) centered at location (x, y), respectively (S4 Fig, together with skewness and kurtosis as the third and fourth standardized moment, respectively, and entropy, $-\sum p \log p$, where p is the probability distribution of the pixel intensity of the image patch); and the asterisk "*" is either "UV" or "Green" indicating the channel identity (Fig 4A,B). Chromatic

Abballe and Asari

contrast C(x, y) was then defined as a difference of the RMS contrasts between the two channels (Fig 4C,D):

$$\mathbf{C}(x,y) = \mathbf{C}_{\mathrm{RMS}}^{\mathrm{UV}}(x,y) - \mathbf{C}_{\mathrm{RMS}}^{\mathrm{Green}}(x,y).$$
(5)

9

For quantification, we fitted the Weibull distribution (Eq.(3)) to the left (C < 0) and right (C > 0) sides of the chromatic contrast distributions separately (Fig 4E,F).

214 **Power spectral density**

The power spectral density of the normalized intensity image I(x, y) was computed with the fast Fourier transform (FFT; Fig 5):

$$F(\omega_x, \omega_y) = \operatorname{FFT}\left[I(x, y)\right] \tag{6}$$

$$S(\omega_x, \omega_y) = F(\omega_x, \omega_y) F^*(\omega_x, \omega_y), \tag{7}$$

where the superscript * denotes complex conjugate, and ω_x and ω_y represent the horizontal and vertical spacial frequency (ranging from -0.5 to 0.5 cycles/pixel), respectively. As the average power spectrum of natural images generally falls with a form $1/f^{\alpha}$ over the spatial frequency *f* with a slope $\alpha \sim 2$ [1, 40, 41], we fitted the power function b/ω^a to $S(\omega_x, 0)$ and $S(0, \omega_y)$, where *a* and *b* indicate the slope and *Y*-intercept in the log-log space. We used a sign-test to compare these parameter values between UV and green channels (Fig 5I–P).

223 Spatial autocorrelation

Following the Wiener–Khinchin theorem, the spatial autocorrelation R(x, y) was computed with the inverse FFT of $S(\omega_x, \omega_y)$ in Eq.(7):

$$R(x, y) = \text{IFFT}\left[S(\omega_x, \omega_y)\right],\tag{8}$$

where x and y represent horizontal and vertical distances of the two pixel points in the target image, respectively (Fig 6). Sign-tests were used to compare the $R(d_h, d_v)$ values at representative data points: $[d_h, d_v] = [0, 50], [50, 0]$ (Fig 6I–L).

Abballe and Asari

10

229 **Results**

230 Multi-spectral camera for the mouse vision

The mouse retina expresses short (S)- and middle (M)-wavelength sensitive opsins that are 231 maximally sensitive to ultraviolet (UV; \sim 360 nm) and green (\sim 508 nm) wavelengths of light, 232 respectively [9–11]. Existing public databases of natural scenes contain a diverse set of images 233 including both natural and artificial objects in both gray and color scales visible to humans [e.g., 234 42-45], but only a handful cover UV images [22-24]. To examine the natural image statistics of 235 the mouse vision, especially for those of the upper and lower visual fields to test the optimality 236 of the dorsoventral functional division of the mouse retina [9, 10, 18–20], we set out to build 237 a multi-spectral camera system for acquiring images of the same scenes in both UV and green 238 spectral domains (Fig 1). 239

We first modelled the spectral sensitivity of the mouse dichromatic vision to determine the 240 center wavelengths of the two channels. Because the lens and cornea absorb shorter wavelength 241 light (e.g., UV rays) more than longer wavelength light, we corrected the absorption spectra 242 of the mouse cone photoreceptors [31] with the transmission spectra of the whole eye optics 243 [30]. This resulted in a slight shift of the center wavelengths to a longer wavelength by several 244 nanometers: from \sim 360 nm to \sim 365 nm for the S-cone and from \sim 508 nm to \sim 512 nm for 245 the M-cone (Fig 1B). Thus, the ocular transmittance had only minor effects on the spectral 246 sensitivity of the mouse vision, reassuring its sensitivity to near-UV light [20, 46]. 247

We then designed a multi-spectral camera system accordingly using a beam-splitting 248 strategy [Fig 1A; see Methods for specifications; 25, 26]. By convolving the measured 249 transmission spectrum of the camera optics with the sensitivity spectrum of the camera 250 sensors [29], we identified that our imaging device had the sensitivities to \sim 368±10 nm and 251 \sim 500 \pm 30 nm (center wavelength \pm half-width at half maximum; HWHM) for the UV and 252 green channels, respectively (Fig 1B). This confirms that the UV and green channels of our 253 device were spectrally well isolated, and that the two channels largely matched to the spectral 254 sensitivity of the mouse vision [9–11]. 255

Abballe and Asari

11

²⁵⁶ Ultraviolet and green image collection

To collect images that mice would encounter in their natural habitats, we went out to natural 257 fields and wild forests in the countryside and mountain area of Lazio/Abruzzo regions in Italy 258 across different seasons. We placed the multi-spectral camera on the ground at about a height of 259 the mouse eye, and acquired images of natural objects alone at various distances (e.g., clouds, 260 trees, flowers, and animals), excluding any artificial objects. These images were taken with 261 different camera angles in the presence of ample natural light (S1 Fig). The images were 262 preprocessed to correct optical vignetting and remove salt-and-pepper noise, and cropped to 263 exclude areas out of focus on the edges (see Methods for details). This led to a set of 232 pairs 264 of UV and green images of various "mouse-view" natural scenes. 265

Besides well-known facts that UV light is reflected well by open water and some plants 266 [13, 14], we noticed several distinct features between the UV and green images (see examples 267 in Fig 2). First, clouds often appeared dark and faint in the UV images than in the green ones. 268 In some cases, even negative contrast was formed for the clouds in UV while positive contrast 269 in green. Second, fine textures were more visible in the green images than in the UV ones. In 270 particular, objects in the upper field UV images were often dark in a nearly uniform manner due 271 to back-light, whereas fine details of the objects were nevertheless visible in the corresponding 272 green images despite a high contrast against the sky. For the lower field images, in contrast, 273 distinct brighter spots stood out in UV due to reflections of shiny leaves and cortices, while 274 more shades and shadows were visible in green. These qualitative observations already suggest 275 that the UV and green images have distinct statistical properties. 276

277 Normalized intensity and contrast distributions of UV and green images

To analyze the image statistics more formally, we first calculated the normalized intensity distribution of the UV and green channels for the upper and lower visual field images (Fig 3A,B). Because the visual system adapts its sensitivity to the range of light intensities in each environment [38, 39], we normalized the pixel intensity of each UV and green image to be within the range from zero to unity. We then found that, for the upper visual field images, the probability distributions of both UV and green intensity values were bimodal (Fig 3A). The

Abballe and Asari

12

two peaks of the UV intensity distribution, however, were higher and more separated than those of the green intensity distribution, suggesting that luminance contrast is higher in UV than in green when animals look up. In contrast, the normalized intensity distributions of the lower field images were unimodal and skewed to the right for both color channels. The distribution was more strongly heavy-tailed for the green than for the UV images (Fig 3B), indicating higher contrast in green than in UV when animals look down.

To better examine the contrast in the two different spectral domains, we calculated the 290 local image contrast using the second derivative (Laplacian) of a two-dimensional Gaussian 291 filter (Eq.(2) in Methods). This filter follows the antagonistic center-surround receptive fields 292 of early visual neurons [e.g., retinal ganglion cells; 47, 48] that are sensitive to local contrast, 293 and is commonly used for edge detection in computer vision [49-51]. Consistent with what 294 was implicated by the intensity distributions (Fig 3A,B), we found that 1) the probability 295 distribution of local contrast was generally wider for the upper visual field images than for 296 the lower visual field images; and 2) the local contrast distribution was wider for the upper 297 visual field UV images than for the corresponding green images (Fig 3C and S3A,C,E Fig), 298 but narrower for the lower visual field UV images than for the green counterparts (Fig 3D 299 and S3B,D,F Fig). To quantify these differences, we fitted a two-parameter Weibull function 300 (Eq.(3) in Methods) to the local contrast distribution of each image in each channel [52, 53], 301 where the first scale parameter (β) describes the width of the distribution, hence a larger value 302 indicating higher contrast; and the second shape parameter (γ) relates to the peakedness, with 303 a smaller value indicating a heavier tail and thus higher contrast in the image. For the images 304 above the horizon, the UV channel had significantly smaller shape parameter values than the 305 green channel (Fig 3G) with comparable scale parameter values (Fig 3E). In contrast, for the 306 images below the horizon, the green channel had significantly larger scale parameter values than 307 the UV channel (Fig 3F), with no difference in the shape parameter values (Fig 3H). Thus the 308 image statistics showed distinct characteristics between the upper and lower visual field image 309 data sets, with higher contrast in UV than in green for the upper visual field images, and vice 310 versa for the lower visual field images. 311

Abballe and Asari

13

Importantly, such differences in the local contrast distributions do not agree well with what 312 the efficient coding hypothesis implies from the physiological and anatomical properties of 313 the mouse retina [3, 4]. Solely from an information theoretic viewpoint, a narrower contrast 314 distribution is better encoded with a more sensitive cone type to maximize its bandwidth [54]. 315 In the mouse retina, the functional S-cones are more sensitive to contrast than the functional M-316 cones [17-20, 46]; and the functional S-cones are denser towards the ventral part of the retina, 317 preferentially sampling the upper part of the visual field, while the functional M-cones towards 318 the dorsal retina, sampling the lower visual field [15, 16, 18]. Therefore, this particular retinal 319 organization is optimal if the upper visual field images had lower contrast in UV than in green, 320 and the lower visual field images had higher contrast in UV than in green. Our image analysis, 321 however, showed the opposite trend in the "mouse-view" visual scenes (Fig 3). 322

323 Achromatic and chromatic contrast of "mouse-view" images

To examine achromatic and chromatic contrast of our image data sets, we next measured the 324 root mean square (RMS) contrast (Eqs.(4) and (5) in Methods) that is commonly used in 325 psychophysical studies [22]. We found that the achromatic RMS contrast (Eq.(4)) was higher in 326 UV than in green channels, especially for the upper visual field images (Fig 4A,B). The upper 327 visual field images then had an asymmetric chromatic contrast distribution (Eq.(5); Fig 4C), 328 where pixels with higher contrast in UV than in green were more abundant than those with 329 higher contrast in green than in UV (Fig 4E,F). In contrast, the chromatic contrast distribution 330 was rather symmetric for the lower visual field images (Fig 4D), and it was overall wider than 331 that for the upper visual field images (Fig 4E,F). 332

This indicates that UV-green chromatic information exists across the visual field, even though the exact shape of the chromatic contrast distribution may depend on the image contents [22]. We indeed identified UV-green chromatic objects in both lower and upper visual field images (see examples in Fig 2 and S2 Fig) and thus cannot explain why the mouse retina has chromatic circuitry preferentially on the ventral side (upper visual field) [55–57]. In principle, mice could retrieve UV-green chromatic information across the visual field, given that 1) genuine S-cones and rods are distributed rather uniformly across the mouse retina [34]; 2) rods

Abballe and Asari

14

have similar absorption spectra to M-cones (peak sensitivity at 498 and 508 nm, respectively;
Fig 1B) [9, 32]; and 3) rods can escape from saturation even under photopic conditions
[33]. Larger image datasets sampled under more diverse conditions are required to assess the
optimality of the chromatic circuitry in the mouse retina, especially because the rod system
plays a role not only in the color vision but also in the scotopic vision.

³⁴⁵ Power spectrum and autocorrelation of UV and green images

We next analyzed the second-order statistics of the acquired images. Specifically, we computed 346 the power spectrum (Fig 5) and spatial autocorrelation that describes the relationship of the 347 two pixel intensity values as a function of their relative locations in the images (Fig 6; see 348 Methods for details). As expected [1, 21], the power spectra generally followed $1/\omega^a$ on the 349 spatial frequency ω for both UV and green channels irrespective of the camera angles (in log-350 log axes; Fig 5A–H); and were higher for the vertical direction than for the horizontal direction 351 (Fig 5A–H)—i.e., the spatial autocorrelation was elongated in the vertical direction (Fig 6A–D). 352 There are, however, several distinct properties between the UV and green channels for the 353 upper and lower visual field images. First, the slope of the power spectra a was larger for the 354 lower visual field images than for the upper visual field images (Fig 5I-L); equivalently, the 355 spatial autocorrelation was narrower for the lower visual field images (Fig 6E–H), indicating the 356 presence of more fine textures in those images. Second, for the upper visual field images, the UV 357 power spectra were higher than the green ones in both vertical and horizontal directions (e.g., 358 the Y-intercept b, indicating the log-power at the spatial frequency of 1 cycle/pixel; Fig 5M,N). 359 In contrast, for the lower visual field images, the UV power spectra were lower with a larger 360 slope than the green counterparts (Fig 5K,L,O,P). Equivalently, the spatial autocorrelation was 361 wider in UV than in green for the upper visual field images, and vice versa for the lower visual 362 field images (Fig 6E–H). 363

³⁶⁴ Under an efficient coding hypothesis, a higher spatial autocorrelation implies that less cones ³⁶⁵ are needed to faithfully encode the scenes [3, 4, 54]. One would then expect from the "mouse-³⁶⁶ view" image statistics that the functional S- and M-cones should be denser on the dorsal and ³⁶⁷ ventral parts of the mouse retina, respectively, to achieve an optimal sampling. However, the

Abballe and Asari

15

opposite is the case with the mouse retina [15, 16, 18], suggesting that the cone distribution bias
 in the mouse retina cannot be simply explained by the optimality principle from an information
 theoretic viewpoint.

371 Discussion

To study the natural image statistics for the mouse vision, here we collected a set of 232 "mouse-372 view" two-color images of various natural scenes across different seasons using a custom-373 made multi-spectral camera (Figs 1 and 2). We identified distinct image statistics properties 374 for the two channels between the images above and below the horizon (Figs 3-6 and S4 Fig). 375 Specifically, both the local contrast and the spatial autocorrelation were higher in UV than in 376 green for the upper visual field images, while they were both lower in UV than in green for 377 the lower visual field images. This disagrees with what the efficient coding hypothesis implies 378 [3, 4] from the functional division of the mouse retina along the dorsoventral axis [15, 16, 18]. 379 We thus suggest that the given retinal organization in mice should have evolved not only to 380 efficiently encode natural scenes from an information theoretic perspective, but likely to meet 38 some other ethological demands in their specific visual environments [22]. 382

How faithful are our images to what mice actually see in their natural habitats? This is a 383 critical question because image statistics depend on the quality and contents of the images. Our 384 camera system was designed to collect high-quality UV-green images (Figs 1 and 2) comparable 385 to the existing natural image datasets for human vision [42–45]. However, caveats include that 386 1) the effects of the mouse eye optics were not considered in the image acquisition or analysis; 387 2) no motion dynamics were considered; 3) images were taken under ample light during the day, 388 while mice are nocturnal; and 4) our image datasets were still relatively small and did not cover 389 the entire visual field for the mouse vision. It is a future challenge to address these questions, 390 for example, by measuring the properties of the mouse eye optics, simulating images projected 391 onto the mouse retina, and analyzing the statistics of these images. 392

Abballe and Asari

16

³⁹³ "Mouse-view" natural image database

We employed a beam-splitting strategy to simultaneously acquire UV and green images of 394 the same scenes (Fig 1) because it has certain advantages over other hyper- or multi-spectral 395 imaging techniques [25, 26]. First, a previous study used a hyperspectral scanning technique 396 where a full spectrum of each point in space was measured by a spectrometer [18]. While the 397 photoreceptor response could be better estimated by using its absorption spectra, the scanned 398 images through a pinhole aperture inevitably had lower spatial and temporal resolutions than 399 the snapshot images acquired with our device. Second, a camera array can be used for multi-400 spectral imaging with each camera equipped with appropriate filters and lenses [58]. This 401 is easy to implement and will perform well for distant objects; however, because angular 402 disparity becomes larger for objects at a shorter distance, one would have a difficulty in taking 403 close-up images that small animals such as mice would normally encounter in their everyday 404 lives. Finally, our single-lens-two-camera design is simple and cost-effective compared to other 405 snapshot spectral imaging methods [26]. In particular, commercially available devices are often 406 expensive and inflexible, hence not suitable for our application to collect images that spectrally 407 match the mouse vision. 408

There are several conceivable directions to expand the "mouse-view" natural image 409 database. First, we could take high dynamic range images using a series of different exposure 410 times. This works only for static objects, but can be useful to collect images at night during 411 which nocturnal animals such as mice are most active. Second, we could take a movie to analyze 412 the space-time statistics of natural scenes [22]. It would be interesting to miniaturize the device 413 and mount it on an animal's head to collect time-lapse images with more natural self-motion 414 dynamics [59, 60]. Expanding our "mouse-view" natural image datasets will be critical to better 415 understand the visual environment of mice and develop a theoretical explanation on species-416 specific and non-specific properties of the mouse visual system. 417

418 Optimality of the mouse retina

⁴¹⁹ What selective pressures have driven the mouse retina to favour UV sensitivity over blue and ⁴²⁰ evolve the dorsoventral gradient in the opsin expression? Our image analysis suggests that

Abballe and Asari

17

the coding efficiency alone with respect to the natural image statistics cannot fully explain 421 the distinctive organization of the mouse retina (Figs 3-6). For example, we argued from an 422 information theoretic viewpoint that, for equalizing the bandwidth within the system, high 423 contrast images in the upper visual field (Fig 3C) should be encoded with less sensitive 424 photoreceptors (M-cones), while low contrast images in the lower visual field (Fig 3D) with 425 more sensitive photoreceptors (S-cones) [18]. In contrast, one could also argue from an 426 ethological viewpoint that more sensitive S-cones should be driven more strongly by high 427 contrast images in the upper visual field and thus better suited to process biologically relevant 428 information, such as aerial predators [2, 22]. 429

To understand in what sense the moues retina's organizations are optimal, one then needs to 430 clarify visual ethological demands that are directly relevant for survival and reproduction. For 43 example, fresh mouse urine reflects UV very well, and this has been suggested to serve as a con-432 specific visual cue for their territories and trails besides an olfactory cue [61]. The UV sensitivity 433 can also be advantageous for the hunting behavior of mice because many nocturnal insects are 434 attracted to UV light. Furthermore, increased UV sensitivity in the ventral retina may improve 435 the detection of tiny dark spots in the sky, such as aerial predators [62]. Indeed, the S-opsin-436 dominant cones in mice have higher sensitivity to dark contrasts than the M-opsin-dominant 437 ones [18], and turning the anatomical M-cones into the functional S-cone by co-expressing the 438 S-opsin will dramatically increase the spatial resolution in the UV channel because the mouse 439 retina has only a small fraction of the uniformly distributed genuine S-cones (~ 5 %) compared 440 to the co-expressing cones [\sim 95 %; 11, 16, 17, 63]. 441

These arguments, however, are difficult to generalize because each species has presumably 442 taken its own strategy to increase the fitness in its natural habitat, leading to convergent and 443 divergent evolution. On the one hand, UV sensitivity was identified in some mammals that live 444 in a different visual environment than mice, including diurnal small animals such as the degu 445 and gerbil [61, 64, 65] and even large animals such as the Arctic reindeer [66]. On the other 446 hand, some species showing a similar behavioral pattern as mice do not have the dorsoventral 447 division of the retinal function [12–14]. For example, even within the genus Mus, some species 448 do not have the dorsoventral gradient of the S-opsin expression, and others completely lack the 449

Abballe and Asari

S-cones [67]. It is even possible that the cone distribution bias may have nothing to do with the perception of the color vision, but may arise just because of the developmental processes. Indeed, the center of the human fovea is generally devoid of S-cones [68, 69], and there is a huge diversity in the ratio of M- and L-cones in the human retina across subjects with normal color vision [70, 71]. Behavioral tests across species will then be critical for validating the ethological arguments to better understand the structure and function of the visual system [2]. We expect that the "mouse-view" natural image datasets will contribute to designing such studies.

457 Figure legends

458 Fig 1: Multi-spectral camera system for the mouse vision

(A) Schematic diagram of the camera optics. Incoming light was split into UV and Green channels by a dichroic mirror and further filtered to match the spectral sensitivity of the mouse visual system (see panel B). A neutral density filter with the optical density value from 1.0 to 2.0 was used for the Green channel to maximize the dynamic range of the camera sensor to be used with the same parameter settings as the UV channel. The inset shows the pixel intensity values as a function of the exposure time (mean \pm standard deviation; N=2,304,000 pixels), supporting the linearity of the camera sensor (Sony, IMX174 CMOS).

(**B**) Relative spectral sensitivity of the camera system (UV channel, violet area; Green channel, green area). For comparison, the spectral sensitivity of the mouse rod and S- and Mcone photoreceptors [31] corrected with the transmission spectrum of the mouse eye optics [30] was shown in black, violet and green lines, respectively, as well as typical sunlight spectrum in gray.

471 Fig 2: Representative images of the natural scenes in UV and green 472 channels

⁴⁷³ See S2 Fig for the UV-Green pixel intensity distribution of these example images.

Abballe and Asari

(A) Upper visual field images taken with positive camera elevation angles (UV, Green, and
pseudo-color merged images from left to right). These images typically contain trees and
branches with sky backgrounds.

(B) Lower visual field images taken with negative camera elevation angles, often containing
a closer look of grasses and flowers.

Fig 3: Light intensity and local contrast distributions of the "mouse-view" natural images

(A,B) Normalized light intensity distributions of the upper (A) and lower (B) visual field
images for UV (violet) and Green (green) channels (median and interquartile range).

(C,D) Local contrast distributions computed with the Laplacian-of-Gaussian filter ($\sigma = 10$ in Eq.(2); see S3 Fig for contrast distributions computed with different σ values). The distribution of the UV channel is more strongly heavy-tailed than that of the Green channel for the upper visual field images (C), but the Green channel's distribution is wider than the UV channel's for the lower visual field images (D).

(E–H) Scale (β ; E,F) and shape (γ ; G,H) parameters from the Weibull distribution fitted to each image (Eq.(3); see Methods for details). For the upper field images (E,G), the UV channel has significantly smaller γ (G) but comparable β (E) values than the Green channel. In contrast, for the lower field images (F,H), the Green channel has significantly larger β (F) but comparable γ (H) values than the UV channel. *P*-values are obtained from sign-tests.

Fig 4: Achromatic and chromatic contrast of the "mouse-view" natural images

⁴⁹⁵ (**A**,**B**) Root mean square (RMS) contrast of the upper (A) and lower (B) field images, ⁴⁹⁶ computed independently for the UV (violet) and Green (green) channels of each image (local

Abballe and Asari

20

⁴⁹⁷ patch size, 30 pixel radius; Eq.(4) in Methods). The UV channel has higher achromatic contrast, ⁴⁹⁸ especially for the upper visual field images (median \pm interquartile range).

(C,D) Chromatic contrast distributions (median \pm interquartile range) computed as a difference of the RMS contrasts between the UV and Green channels (Eq.(5) in Methods). The distribution was asymmetric for the upper field images (C) but rather symmetric for the lower field images (D).

(E,F) Scale (β ; E) and shape (γ ; F) parameters from the Weibull distribution (Eq.(3)) fitted to each side of the chromatic contrast distribution of each image. The box plot shows the median \pm interquartile range. The upper field images contain fewer pixels that have higher contrast in Green than in UV (rank-sum test: three stars " $\star \star \star$ " indicating p < 0.001; $\star \star$, p < 0.01; and \star , p < 0.05).

⁵⁰⁸ Fig 5: Power spectrum of the "mouse-view" natural images

(A–D) The average power spectra of the upper (A,B) and lower (C,D) visual field images for the UV (A,C) and Green (B,D) channels.

⁵¹¹ (E–H) The power spectra in the vertical (E,G) and horizontal (F,H) directions (median and ⁵¹² interquartile range) for the upper (E,F) and lower (G,H) visual field images.

⁵¹³ (I–M) The slope (a; I–L) and Y-intercept (b; M–P) parameters of the power function b/ω^a ⁵¹⁴ in the log-log space fitted to the power spectra of each image in the vertical (I,K,M,O) and ⁵¹⁵ horizontal (J,L,N,P) directions. For the upper visual field images (I,J,M,N), the UV channel ⁵¹⁶ has significantly larger b (M,N) but comparable a (I,J) values than the Green channel. For the ⁵¹⁷ lower field images (K,L,O,P), in contrast, the Green channel has significantly larger b (O,P) and ⁵¹⁸ smaller a (K,L) values than the UV channel. P-values are obtained from sign-tests.

Abballe and Asari

21

Fig 6: Spatial autocorrelation of the "mouse-view" natural images

 $_{520}$ (A–D) The average spatial autocorrelation of the upper (A,B) and lower (C,D) visual field $_{521}$ images for the UV (A,C) and Green (B,D) channels, respectively.

(E–H) The spatial autocorrelation in the vertical (E,G) and horizontal (F,H) directions (median and interquartile range). The UV channel has a higher and wider spatial correlation for the upper visual field images (E,F), while the Green channel has a higher and wider spatial correlation for the lower visual field images (G,H).

 $_{526}$ (I–L) Representative spatial correlation values of the pixels horizontally (I,K) or vertically $_{527}$ (J,L) separated by 50 pixels for the upper (I,J) and lower (K,L) visual field images. *P*-values were obtained from sign-tests.

Supporting information

530 S1 Fig: Relative pixel intensities along horizontal and vertical axes

Relative pixel intensities (median \pm interquartile range; UV and green channels in violet and 531 green, respectively) were computed along horizontal (A,C,E) and vertical (B,D,F) axes for three 532 different image categories based on the camera angle: lower (A,B; N = 117), horizontal (C,D; 533 N = 15), and upper (E,F; N = 100) visual field images. Pixel intensity did not change much 534 horizontally but was generally lower in the lower field images (A,B) than in the upper field 535 images (E,F). Discontinuity between the top edge of the lower field images (B, X-axis value 536 of 0) and the bottom edge of the upper field images (F, X-axis value of 0) supports a good 537 separation of the two image categories. 538

Abballe and Asari

22

S2 Fig: UV-Green pixel intensity distributions of representative "mouse view" images

Each scatter plot shows the distribution of the UV-Green pixel values from the corresponding image shown in Fig 2 (A, upper visual field images; B, lower visual field images). Virtually all pixels were within the dynamic range of the camera sensor (Sony, IMX174 CMOS; 12-bit depth saved in a 16-bit format).

545 S3 Fig: Local contrast distributions of the natural scenes are scale invariant

Local contrast distributions computed with different Laplacian-of-Gaussian filter sizes (A,B, $\sigma = 5$; C,D, $\sigma = 20$; E,F, $\sigma = 40$; Eq.(2)) are shown in the same format as Fig 3C,D ($\sigma = 10$). The upper visual field images (A,C,D) generally showed higher contrast than the lower visual field images (B,D,F), especially for the UV channel (violet). The filter size (0.18–1.44 degrees) used in this study is smaller than the receptive field size of mouse retinal ganglion cells (3-13 degrees) [72, 73]. Given the scale invariance [1, 21], however, we expect that our analysis results should hold for larger filters as well [22].

S4 Fig: Natural image statistics for "mouse-view" images have distinct spectral properties between upper and lower visual fields across different order statistics

The first- to the fourth-order image statistics (mean, A, B; standard deviation, C, D; skewness, E, F; kurtosis, G, H) as well as entropy (I, J) were computed for local images patches (0.36 degrees; UV, violet; Green, green). Joint (top) and marginal (bottom) probability distributions were then generated for the upper (A, C, E, G, I) and lower (B, D, F, H, J) visual field images.

23

Abballe and Asari

560 **References**

- [1] Simoncelli EP, Olshausen BA. Natural image statistics and neural representation. Annu
 Rev Neurosci. 2001;24:1193–1216.
- ⁵⁶³ [2] Baden T, Euler T, Berens P. Understanding the retinal basis of vision across species. Nat
 ⁵⁶⁴ Rev Neurosci. 2020;21:5–20.
- [3] Attneave F. Some informational aspects of visual perception. Psychol Rev. 1954;61:183–
 193.
- ⁵⁶⁷ [4] Barlow HB. Possible principles underlying the transformation of sensory messages. In:
 ⁵⁶⁸ Rosenblith WA, editor. Sensory Communication. MIT Press; 1961. p. 217–234.
- ⁵⁶⁹ [5] Gjorgjieva J, Sompolinsky H, Meister M. Benefits of pathway splitting in sensory coding.
 ⁵⁷⁰ J Neurosci. 2014;34:12127–12144.
- [6] Olshausen BA, Field DJ. Emergence of simple-cell receptive field properties by learning
 a sparse code for natural images. Nature. 1996;381:607–609.
- 573 [7] Smith E, Lewicki M. Efficient auditory coding. Nature. 2006;439:978–982.
- [8] Huberman AD, Niell CM. What can mice tell us about how vision works? Trends
 Neurosci. 2011;34:464–473.
- ⁵⁷⁶ [9] Jacobs GH, Neitz J, Deegan II JF. Retinal receptors in rodents maximally sensitive to
 ⁵⁷⁷ ultraviolet light. Nature. 1991;353:655–656.
- [10] Lyubarsky A, Falsini B, Pennesi M, Valentini P, Pugh Jr E. UV- and midwave-sensitive
 cone-driven retinal responses of the mouse: a possible phenotype for coexpression of cone
 photopigments. J Neurosci. 1999;19:442–455.
- [11] Nikonov S, Kholodenko R, Lem J, Pugh Jr E. Physiological features of the S-and
 M-cone photoreceptors of wild-type mice from single-cell recordings. J Gen Physiol.
 2006;127:359–374.

Abballe and Asari

24

- [12] Peichl L. Diversity of mammalian photoreceptor properties: adaptations to habitat and
 lifestyle? Anat Rec A Discov Mol Cell Evol Biol. 2005;287:1001–1012.
- [13] Cronin TW, Bok MJ. Photoreception and vision in the ultraviolet. J Exp Biol.
 2016;219:2790–2801.
- [14] Hunt DM, Wilkie SE, Bowmaker JK, Poopalasundaram S. Vision in the ultraviolet. Cell
 Mol Life Sci. 2001;58:1583–1598.
- [15] Szél A, Röhlich P, Caffé AR, Juliusson B, Aguirre G, Van Veen T. Unique topographic
 separation of two spectral classes of cones in the mouse retina. J Comp Neurol.
 1992;325:327–342.
- [16] Applebury ML, Antoch MP, Baxter LC, Chun LL, Falk JD, Farhangfar F, et al. Cone
 photoreceptor: a single cone type expresses both S and M opsins with retinal spatial
 patterning. Neuron. 2000;27:513–523.
- [17] Röhlich P, Van Veen T, Szél A. Two different visual pigments in one retinal cone cell.
 Neuron. 1994;13:1159–1166.
- [18] Baden T, Schubert T, Chang L, Wei T, Zaichuk M, Wissinger B, et al. A tale of two
 retinal domains: Near-optimal sampling of achromatic contrasts in natural scenes through
 asymmetric photoreceptor distribution. Neuron. 2013;80:1206–1217.
- [19] Wang YV, Weick M, Demb JB. Spectral and Temporal Sensitivity of Cone-Mediated
 Responses in Mouse Retinal Ganglion Cells. J Neurosci. 2011;31:7670–7681.
- [20] Jacobs GH, Williams GA. Contributions of the mouse UV photopigment to the ERG and
 to vision. Doc Ophthalmol. 2007;115:137–144.
- [21] Hyvärinen A, Hurri J, Hoyer PO. Natural Image Statistics: A Probabilistic Approach to
 Early Computational Vision. Springer-Verlag London; 2009.
- [22] Qiu Y, Zhao Z, Klindt D, Kautzky M, Szatko KP, Schaeffel F, et al. Mouse retinal
 specializations reflect knowledge of natural environment statistics. Curr Biol. 2021;31:1–
 15.

Abballe and Asari

25

- [23] Differt D, Möller R. Insect models of illumination-invariant skyline extraction from UV
 and green channels. J Theor Biol. 2015;380:444–462.
- ⁶¹² [24] Differt D, Möller R. Spectral skyline separation: extended landmark databases and
 ⁶¹³ panoramic imaging. Sensors. 2016;16:1614.
- ⁶¹⁴ [25] Grahn H, Geladi P. Techniques and Applications of Hyperspectral Image Analysis. John
 ⁶¹⁵ Wiley and Sons; 2007.
- ⁶¹⁶ [26] Hagen N, Kudenov MW. Review of snapshot spectral imaging technologies. Opt Eng.
 ⁶¹⁷ 2013;52:090901.
- [27] Jähne B, Herrmann H. EMVA 1288 datasheet Basler acA1920-155um, 0 dB gain; 2015.

Available from: https://doi.org/10.5281/zenodo.33040.

- [28] Jähne B, Herrmann H. EMVA 1288 datasheet Basler acA1920-155um, 12 dB gain; 2015.
 Available from: https://doi.org/10.5281/zenodo.33041.
- [29] FLIR White Paper: Sony Pregius Global Shutter CMOS Imaging 622 Performance; 2015 (accessed 28-July-2021). Available from: https: 623 //www.flir.com/globalassets/support/iis/whitepaper/ 624
- sony-pregius-global-shutter-cmos-imaging-performance.pdf.
- [30] Henriksson JT, Bergmanson JPG, Walsh JE. Ultraviolet radiation transmittance of the
 mouse eye and its individual media components. Exp Eye Res. 2010;90:382–387.
- [31] Govardovskii VI, Fyhrquist N, Reuter T, Kuzmin DG, Donner K. In search of the visual
 pigment template. Vis Neurosci. 2000;17:509–528.
- [32] Bridges CDB. Visual Pigments of Some Common Laboratory Mammals. Nature.
 1959;184:1727–1728.
- [33] Tikidji-Hamburyan A, Reinhard K, Storchi R, Dietter J, Seitter H, Davis KE, et al. Rods
 progressively escape saturation to drive visual responses in daylight conditions. Nat
 Commun. 2017;8:1813.

Abballe and Asari

- [34] Jeon CJ, Strettoi E, Masland RH. The Major Cell Populations of the Mouse Retina. J
 Neurosci. 1998;18:8936–8946.
- [35] Carter-Dawson LD, LaVail MM. Rods and cones in the mouse retina. I. Structural analysis
 using light and electron microscopy. J Comp Neurol. 1979;188:245–262.
- [36] Bonin V, Mante V, Carandini M. The Statistical Computation Underlying Contrast Gain
 Control. J Neurosci. 2006;26:6346–6353.
- [37] Tkačik G, Ghosh A, Schneidman E, Segev R. Adaptation to changes in higher-order
 stimulus statistics in the salamander retina. PLOS ONE. 2014;e85841.
- [38] Shapley R, Enroth-Cugell C. Visual adaptation and retinal gain controls. Prog Retinal
 Res. 1984;3:263–346.
- [39] Gollisch T, Meister M. Eye Smarter than Scientists Believed: Neural Computations in
 Circuits of the Retina. Neuron. 2010;65:150–164.
- [40] Burton GJ, Moorhead IR. Color and spatial structure in natural scenes. Appl Opt.
 1987;26:157–170.
- [41] Tolhurst DJ, Tadmor Y, Tang C. The amplitude spectra of natural images. Ophthalmic
 Physiol Opt. 1992;12:229–232.
- [42] van Hateren JH, van der Schaaf A. Independent Component Filters of Natural Images
 Compared with Simple Cells in Primary Visual Cortex. Proc Biol Sci. 1998;265:359–366.
- [43] Geisler WS, Perry JS. Statistics for optimal point prediction in natural images. J Vis.
 2011;11:14.
- [44] Tkačik G, Garrigan P, Ratliff C, Milčinski G, Klein JM, Seyfarth LH, et al. Natural Images
 from the Birthplace of the Human Eye. PLOS ONE. 2011;6:1–12.
- [45] Zhou B, Lapedriza A, Xiao J, Torralba A, Oliva A. Learning Deep Features for Scene
 Recognition using Places Database. In: Ghahramani Z, Welling M, Cortes C, Lawrence

Abballe and Asari

659	N, Weinberger KQ, editors. Advances in Neural Information Processing Systems. vol. 27.
660	Curran Associates, Inc.; 2014.

- ⁶⁶¹ [46] Jacobs GH, Williams GA, Fenwick JA. Influence of cone pigment coexpression on
 ⁶⁶² spectral sensitivity and color vision in the mouse. Vision Res. 2004;44:1615–1622.
- [47] Rodieck RW, Stone J. Analysis of Receptive Fields of Cat Retinal Ganlion Cells. J
 Neurophysiol. 1965;28:833–849.
- [48] Enroth-Cugell C, Robson JG. The contrast sensitivity of retinal ganglion cells of the cat.
 J Physiol. 1966;187:517–552.
- [49] Marr D, Hildreth E. Theory of edge detection. Proc R Soc Lond Ser B. 1980;207:187–217.
- ⁶⁶⁸ [50] Ghosh K, Sarkar S, Bhaumik K. Understanding image structure from a new multi-scale
 ⁶⁶⁹ representation of higher order derivative filters. Image Vis Comput. 2007;25:1228–1238.
- ⁶⁷⁰ [51] Lindeberg T. A computational theory of visual receptive fields. Biol Cybern.
 ⁶⁷¹ 2013;107:589–635.
- ⁶⁷² [52] Geusebroek JM, Smeulders AWM. A six-stimulus theory for stochastic texture. Int J
 ⁶⁷³ Comput Vis. 2005;62:7–16.
- ⁶⁷⁴ [53] Gijsenij A, Gevers T. Color Constancy Using Natural Image Statistics and Scene
 ⁶⁷⁵ Semantics. IEEE Trans Pattern Anal Mach Intell. 2011;33:687–698.
- ⁶⁷⁶ [54] Laughlin S. A simple coding procedure enhances a neuron's information capacity. Z
 ⁶⁷⁷ Naturforsch C Biosci. 1981;36:910–912.
- ⁶⁷⁸ [55] Joesch M, Meister M. A neuronal circuit for colour vision based on rod–cone opponency.
 ⁶⁷⁹ Nature. 2016;532:236–239.
- [56] Nadal-Nicolás FM, Kunze VP, Ball JM, Peng BT, Krishnan A, Zhou G, et al. True S cones are concentrated in the ventral mouse retina and wired for color detection in the
 upper visual field. eLife. 2020;9:e56840.

Abballe and Asari

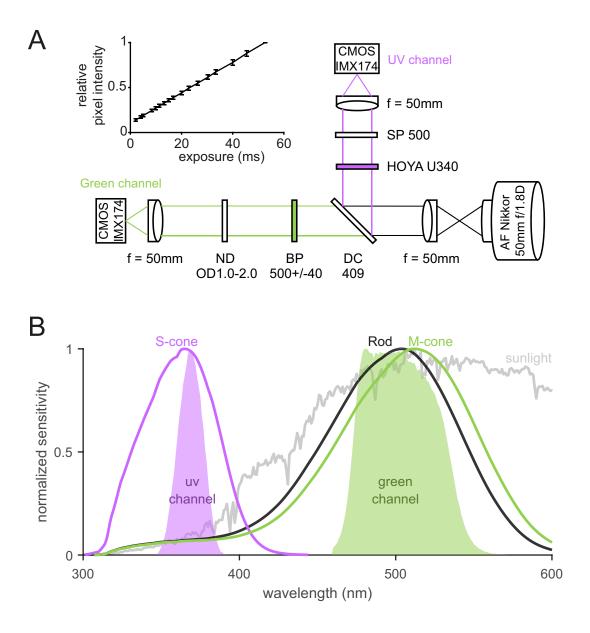
- [57] Szatko KP, Korympidou MM, Ran Y, Berens P, Dalkara D, Schubert T, et al. Neural
 circuits in the mouse retina support color vision in the upper visual field. Nat Commun.
 2020;11:3481.
- [58] Genser N, Seiler J, Kaup A. Camera Array for Multi-Spectral Imaging. IEEE Trans Image
 Process. 2020;29:9234–9249.
- [59] Meyer AF, Poort J, O'Keefe J, Sahani M, Linden JF. A head-mounted camera system
 integrates detailed behavioral monitoring with multichannel electrophysiology in freely
 moving mice. Neuron. 2018;100:46–60.e7.
- [60] Sattler NJ, Wehr M. A Head-Mounted Multi-Camera System for Electrophysiology and
 Behavior in Freely-Moving Mice. Front Neurosci. 2021;24:592417.
- [61] Chàvez AE, Bozinovic F, Peichl L, Palacios AG. Retinal spectral sensitivity, fur coloration
 and urine reflectance in the genus *Octodon* (Rodentia): implications for visual ecology.
 Invest Ophthalmol Vis Sci. 2003;44:2290–2296.
- [62] Yilmaz M, Meister M. Rapid innate defensive responses of mice to looming visual stimuli.
 Curr Biol. 2013;23:2011–2015.
- [63] Haverkamp S, Wässle H, Duebel J, Kuner T, Augustine GJ, Feng G, et al. The primordial,
 blue-cone color system of the mouse retina. J Neurosci. 2005;25:5438–5445.
- [64] Govardovskii VI, Röhlich P, Szél A, Khokhlova TV. Cones in the retina of the Mongolian
 gerbil, *Meriones unguiculatus*: an immunocytochemical and electrophysiological study.
 Vision Research. 1992;32:19–27.
- [65] Jacobs GH, Calderone JB, Fenwick JA, Krogh K, Williams GA. Visual adaptations in a
 diurnal rodent, *Octodon degus*. J Comp Physiol A. 2003;189:347–361.
- [66] Hogg C, Neveu M, Stokkan KA, Folkow L, Cottrill P, Douglas R, et al. Arctic reindeer
 extend their visual range into the ultraviolet. J Exp Biol. 2003;214:2014–2019.
- ⁷⁰⁷ [67] Szél A, Röhlich P, Caffé AR, Van Veen T. Distribution of cone photoreceptors in the
 ⁷⁰⁸ mammalian retina. Microsc Res Techn. 1996;35:445–462.

Abballe and Asari

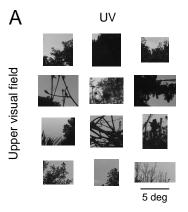
⁷⁰⁹ [68] Wald G. Blue-Blindness in the Normal Fovea. J Opt Soc Am. 1967;57:1289–1301.

- [69] Curcio CA, Allen KA, Sloan KR, Lerea CL, Hurley JB, Klock IB, et al. Distribution and
 morphology of human cone photoreceptors stained with anti-blue opsin. J Comp Neurol.
 1991;312:610–624.
- [70] Roorda A, Williams DR. The arrangement of the three cone classes in the living human
 eye. Nature. 1999;397:520–522.
- [71] Hofer H, Carroll J, Neitz J, Neitz M, Williams DR. Organization of the Human
 Trichromatic Cone Mosaic. J Neurosci. 2005;25:9669–9679.
- [717 [72] Bleckert A, Schwartz GW, Turner MH, Rieke F, Wong ROL. Visual space is represented
- by nonmatching topographies of distinct mouse retinal ganglion cell types. Curr Biol.
 2014;24:310–315.
- [73] Jacoby J, Schwartz GW. Three Small-Receptive-Field Ganglion Cells in the Mouse Retina
 Are Distinctly Tuned to Size, Speed, and Object Motion. J Neurosci. 2017;37:610–625.

Abballe and Asari

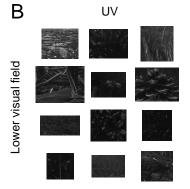


Abballe and Asari





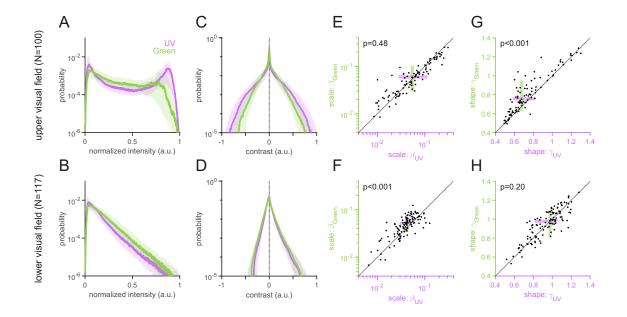




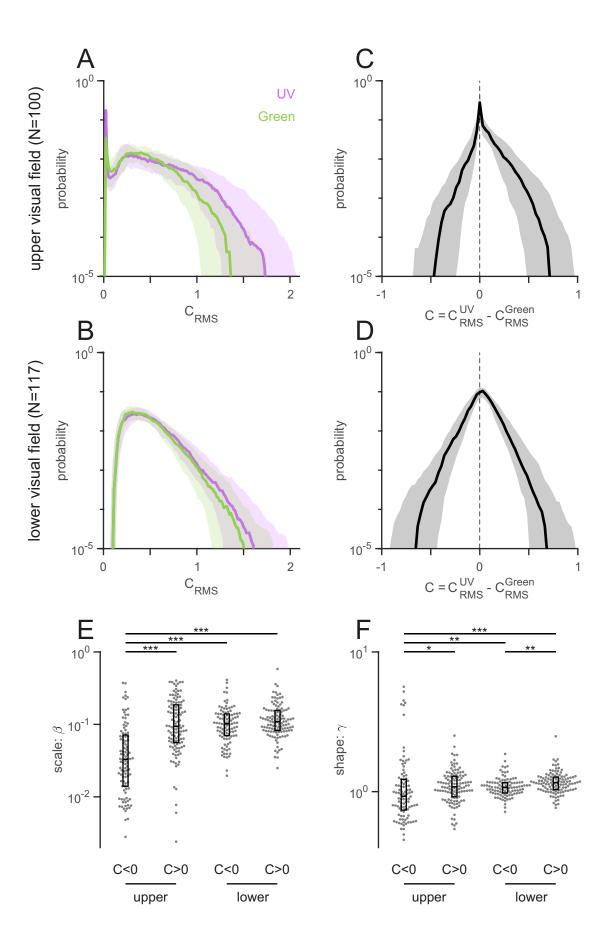
	Green	
		an a
A A A		

Merged			
	-		
He of an			

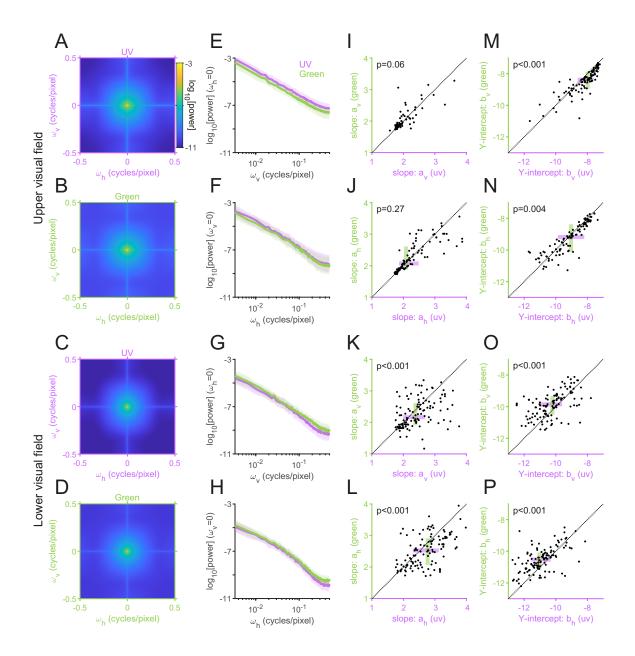
Abballe and Asari



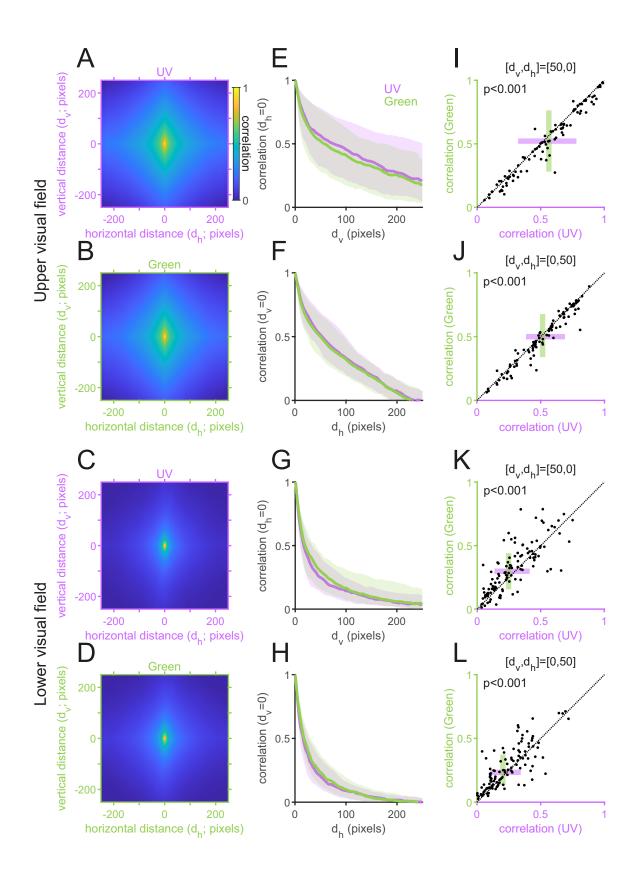
Abballe and Asari



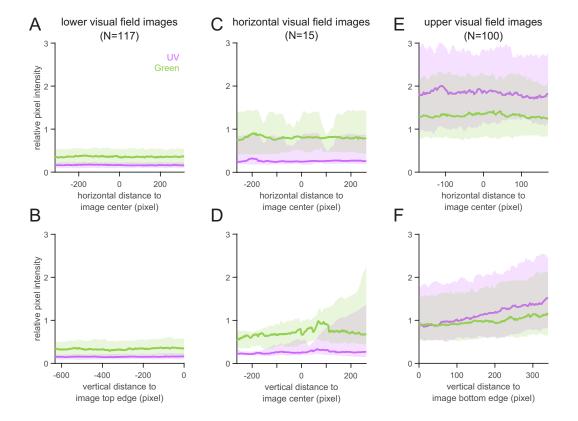
Abballe and Asari



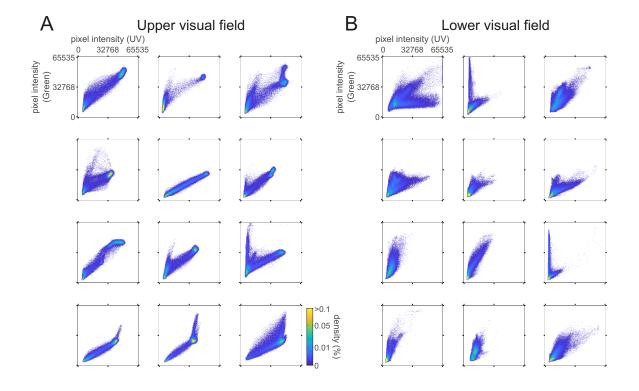
Abballe and Asari



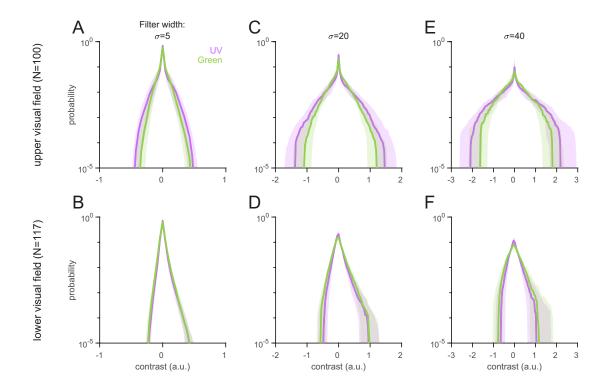
Abballe and Asari



Abballe and Asari



Abballe and Asari



Abballe and Asari

